Momentum Transport by Gravity Waves

JINWON KIM AND L. MAHRT

Department of Atmospheric Sciences, Oregon State University, Corvallis, Oregon

(Manuscript received 18 February 1991, in final form 8 August 1991)

ABSTRACT

The momentum flux by orographic gravity waves and the turbulent heat flux in wave-breaking regions are estimated from aircraft data from ALPEX. The fluxes on 6 March 1982 are controlled by low-level directional shear of the mean flow and associated critical level with wave stress decreasing toward the critical level. On 25 March 1982 a critical level does not occur and wave stress is approximately constant with height within the observational domain. The calculation of these fluxes appears to be the first direct comparison between simple models of gravity-wave momentum flux and observed atmospheric fluxes.

To develop a simple formulation of gravity wave drag for large-scale models, the gravity-wave stress supersaturation theory by Lindzen is generalized for the application to vertically varying mean flows. The wave momentum flux estimated from the generalized model agrees well with the observations for the two ALPEX days. For the 6 March case, the vertical divergence of wave momentum flux below the critical level is comparable to the Coriolis term in the momentum equation. The *effective* height of the surface topography required for the formulation of the wave momentum flux at the ground surface is estimated from the data and found to agree with the formulation of Stern and Pierrehumbert.

Wave breaking below the critical level leads to a convectively unstable region 10–20 km wide where well-organized turbulent-scale convection occurs. The magnitude of the observed upward turbulent heat flux can be approximated by using the flux gradient relationship in which the mixing length and modified shear are derived from the generalized wave-stress supersaturation condition. However, the net turbulent heat flux across the entire width of the mountain waves appears to be small due to cancellation between the upward heat flux in the convectively unstable region and the downward heat flux at the back of the wave. The spatially averaged wave-scale heat flux is also small for the data analyzed here.

1. Introduction

Topographically generated internal gravity waves can transport significant momentum vertically in the atmosphere. The nondissipative nature of internal gravity waves (Eliassen and Palm 1960) may allow the wave stress at the ground surface to be transferred far into the upper atmosphere where the density is small. Wave stress divergence associated with wave breaking acts as a drag on the mean flow at the wave breaking level. The impact of gravity wave drag is known to be especially important for large-scale motions on time scales longer than one week over continental areas during the wintertime (Palmer et al. 1986). Spectral analyses show that the mesoscale variances are climatologically much larger over mountainous areas than over flat land surfaces or the ocean, and the observed differences are mostly due to gravity wave activity in the atmosphere (Jasperson et al. 1990).

Momentum transfer by gravity waves can be locally important on smaller time scales above significant topography. Lilly et al. (1982), Brown (1983), and Hoinka (1985) found that the stress due to gravity-wave-scale disturbances over mountainous areas sometimes exceeds several newtons per square meter in the middle of the troposphere. This value is one or two orders of magnitude larger than typical turbulent stresses in the boundary layer. For a summary of the observed values of the gravity wave stress in previous studies, see Palmer et al. (1986).

Gravity wave drag is usually parameterized in terms of solutions to the linear gravity wave equation with Kelvin-Helmholtz instability or convective instability as a criterion for wave breaking. The modeling study of Klemp and Lilly (1978) shows that a linearized two-dimensional model, combined with an adjustment of local flow with respect to Kelvin–Helmholtz instability, can simulate orographic gravity waves and associated momentum flux reasonably well. Inclusion of gravity wave drag parameterization has been shown to significantly improve the simulation of large-scale flow (Holton 1982; Palmer et al. 1986; McFarlane 1987; Hunt 1990). However, simple formulations of gravity wave momentum flux have, to our knowledge, not been directly compared to observed fluxes. Such comparisons must include the computation of the *effective* height of surface topography, the effects of nonlinear

Corresponding author address: Dr. Larry J. Mahrt, Oregon State University, Department of Atmospheric Sciences, Corvallis, OR 97331-2209.

lower boundary conditions (Smith 1977), and the saturation and supersaturation conditions for the gravity wave stress (Lindzen 1981, 1988). Direct comparison of a gravity wave drag parameterization with observed atmospheric fluxes is one of the main goals of this study.

Representation of the wave breaking process in the frame of linear gravity wave theory plays a central role in the parameterization of gravity wave drag. Lindzen (1981) introduces the wave-stress saturation hypothesis assuming that the maximum amplitude of a gravity wave is limited by the onset of hydrodynamic instability. This wave stress saturation condition has been successfully employed in large-scale modeling studies (Palmer et al. 1986). However, Smith (1977) and Lindzen (1988) suggest that some degree of convective instability can be maintained in wave breaking regions (wave-stress supersaturation hypothesis).

Determination of the wave stress at the ground surface requires the value of the amplitude of the vertical displacement of a streamline at the ground surface (effective mountain height), which is usually assumed to be related to the height of the mountain (or the root-mean-square variance of subgrid-scale orography for large-scale models). The vertical displacement of a streamline at the ground surface also depends on the flow conditions near the ground surface including the flow Froude number (Fr) defined as $\mathrm{Fr} \equiv N_0\eta_0/U_0$, where η_0 is the height of the surface topography, and N_0 and U_0 are the buoyancy frequency and mean wind speed near the ground, respectively (Drazin 1961; Pierrehumbert and Wyman 1986). The nonlinear study of Drazin (1961) shows that as the Froude number increases, the flow near a three-dimensional obstacle becomes more two-dimensional; when the Froude number exceeds unity, the vertical displacement of a streamline is essentially suppressed. Similar features are observed in the three-dimensional numerical modeling studies of Smolarkiewicz and Rotunno (1989). Blocking of the low-level flow upstream from the topography or pooling of cold air in a valley reduces the effective mountain height. However, such processes are nonlinear and have no precise theoretical description. Stern and Pierrehumbert (1988) provide an estimate of the effective mountain height in terms of a critical Froude number based on two-dimensional modeling studies. In this study, we estimate the effective mountain height by fitting the gravity-wave amplitude at the ground with the observed wave stress below the model-predicted wave-breaking level.

The vertical heat flux by breaking gravity waves and associated turbulence may be locally important. Asymmetry of the streamlines due to wave steepening and nonlinear interactions between waves may induce some net wave heat flux. In addition, wave breaking and associated turbulence can cause significant local turbulent heat flux. Earlier parameterizations of wave drag of Lindzen (1981) and Holton (1982) assume that the turbulent Prandtl number in the wave breaking region will be close to unity, that is, heat and momentum transfer in the wave breaking region are of similar efficiency. Chao and Schoeberl (1984) suggest that streamlines will be nearly vertical in the wave breaking region, in which case the local turbulent heat flux is near zero. Fritts and Dunkerton (1985) also suggest small net heat flux across the entire wave due to the upward turbulent heat flux in the convectively unstable wave breaking region. From rotating tank experiments, Delisi and Orlanski (1975) and Dunkerton (1989) observe that wave breaking does not cause significant alteration of the initial stratification implying small net turbulent and wave heat flux.

The spatial variations of the turbulent heat flux will yield important information about the mechanisms of wave breaking. If wave breaking occurs mainly by Kelvin-Helmholtz instability, turbulent heat flux in the wave breaking region is expected to be downward. If wave breaking occurs by convective instability, the turbulent heat flux will be locally upward in the wave breaking region. This phenomenon can offset much of the downward heat flux due to wave-induced turbulence in the stably stratified regions. The observed turbulent heat flux is studied in section 3 using aircraft data from ALPEX (the Alpine Experiment). In section 8, we will formulate the upward turbulent heat flux in terms of wave-modified variables and compare with the observed turbulent heat flux.

Aircraft data collected on 6 and 25 March 1982 in ALPEX are analyzed in sections 2 and 3 in order to study the most important characteristics of the disturbances generated by the underlying coastal range. The analysis will focus on wave momentum fluxes, wave breaking, and resulting turbulent heat flux in the wave breaking region. A simple parameterization of the gravity wave drag is presented in sections 4 and 5 using the solution to the linear gravity wave equation with first-order expansion of a nonlinear lower boundary condition presented in Smith (1977) combined with a generalization of the wave stress supersaturation condition of Lindzen (1988). Lindzen's (1988) theory of supersaturation is derived for an isothermal atmosphere with constant wind speed. We will generalize Lindzen's wave stress supersaturation theory for application to vertically varying mean flows by introducing an *equivalent scale height*, which replaces the scale height for an isothermal atmosphere. In section 6, the vertical profiles of wave momentum flux estimated for the ALPEX cases are compared with the observed wave momentum flux. Inference of the effective mountain height based on model comparisons with the data is presented in section 7.

2. Observed flow

The NCAR Electra aircraft flew over the coastal range of northern Yugoslavia on 6 and 25 March 1982 in the northeast–southwest direction, approximately

parallel to the direction of the low-level wind and perpendicular to the coastal range axis. The flights covered a region approximately 240 km wide, centered at the coastal ridge, in a layer 2.4–5.7 km above sea level. This study analyzes five flight legs at 2.4, 2.7, 3.3, 3.8, and 4.5 km above sea level for 6 March ALPEX and three flight legs at 3.3, 4.5, and 5.7 km above sea level for 25 March ALPEX.

The vertical structure of the mean wind, observed by radiosonde soundings at Zagreb, Yugoslavia, is quite different between the two days (Figs. 1a,c). On 6 March, a strong bora flow near the ground surface leads to significant speed and directional shear. On 25 March, the wind speed increases monotonically in the vertical without significant change of wind direction within the troposphere. Detailed description of the flow on these two days is presented in Smith (1987) and Mahrt and Gamage (1987).

The vertical propagation of orographic gravity waves is influenced by the vertical variation of the wind component parallel to the *surface* wind (McFarlane 1987) defined as

$$\mathbf{V}_p(z) \equiv \frac{\mathbf{V}(z)\cdot\mathbf{V}_0}{|\mathbf{V}_0|}, \tag{1}$$

where $\mathbf{V}_p(z)$ is the mean wind component parallel to the surface wind $\mathbf{V}_0$, $\mathbf{V}(z)$ is the mean wind at height z, and $\mathbf{V}(z)\cdot\mathbf{V}_0$ denotes the scalar product between the two vectors $\mathbf{V}_0$ and $\mathbf{V}(z)$. The *surface* wind directly

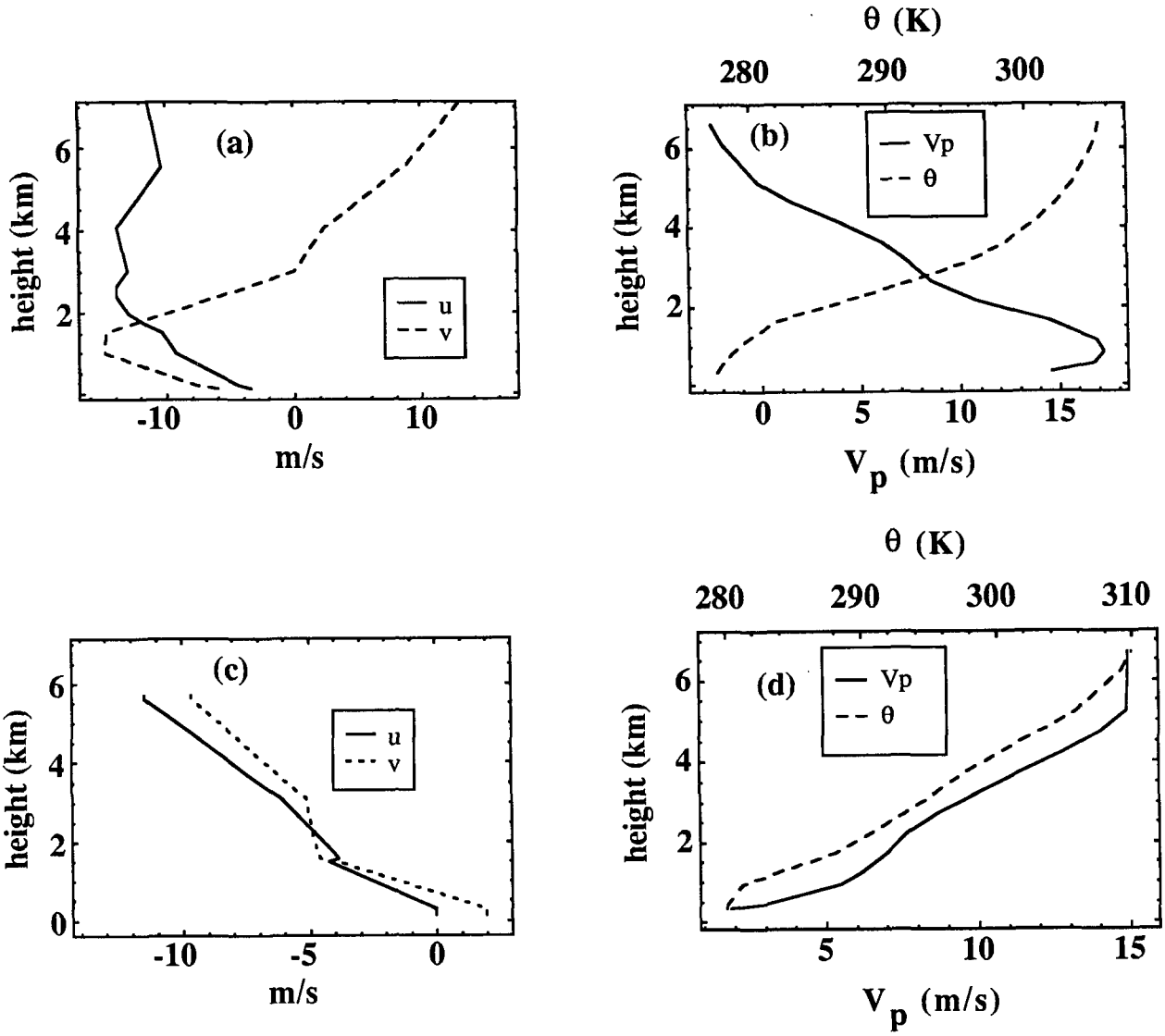

FIG. 1. Vertical profiles of u, v, V_p, and θ from the radiosonde over Zagreb, Yugoslavia, at 1200 LST 6 March 1982 (a,b) and 0900 LST 25 March 1982 (c,d), obtained by averaging the soundings at 0600 and 1200 LST. Heights are with respect to sea level.

responsible for the onset of wave motion is somewhat difficult to define. In this study we use the wind speed from the upstream radiosonde sounding averaged over a 200-m-deep layer centered at the ridge top level.

The observed flow over the mountain range appears to be stationary. On 6 March, V_p decreases with increasing height with a critical level for stationary gravity waves ($V_p = 0$) at 5 km above sea level (Fig. 1b). Vertical decrease of this wind component can cause amplification and breaking of gravity waves as discussed in later sections. In contrast, V_p increases with increasing height and critical layer does not exist within the observational domain for 25 March (Fig. 1d).

Mainly, the flow on 6 March is investigated where low-level wave breaking is expected. The horizontal wind parallel to the direction of the flight, the vertical wind, and the potential temperature observed at the 3.3-km level on 6 March are presented in Fig. 2 together with the underlying topography. The most significant feature of the observed flow is the large-amplitude disturbances on a horizontal scale of a few tens of kilometers accompanied by smaller scale turbulence. The strongest disturbances are confined to the lowest first few kilometers above the coastal range.

The larger-scale motions are isolated by bandpass filtering the raw records with 10- and 80-km cutoff wavelengths for the lower and upper limits of horizontal length scales, respectively. The wavelengths were chosen based on inspection of the record, which includes one major event on the scale of mountain range and smaller-scale wavelike motions. The computed fluxes are not sensitive to the exact values of the cutoff wavelengths. These bandpass-filtered disturbances will be loosely called the *wave-scale* disturbances. Noticeable peaks of the variance of wave-scale vertical velocity appear above and immediately downstream from the ridge (Fig. 3). Growth and breaking of gravity waves are usually accompanied by significant asymmetry of the shape of perturbation streamlines and the concentrated horizontal gradients of u. Such sharp gradients appear as boundaries of ramp-like structures and may indicate the presence of a *frontal* region associated with wave steepening. The strongest events in the records of u and w at the 3.3-km flight level (Fig. 2) are examples of such a structure.

The turbulence occurring on 6 March is strongly related to wave-scale motions. The variance of 1-km high-pass–filtered vertical velocity (Fig. 3) is large at locations of large wave-scale variance. Turbulence in the wave breaking regions and associated turbulent heat flux will be discussed in more detail in section 8. Similar horizontal variations occur at other flight levels near and below the critical level on 6 March (not shown).

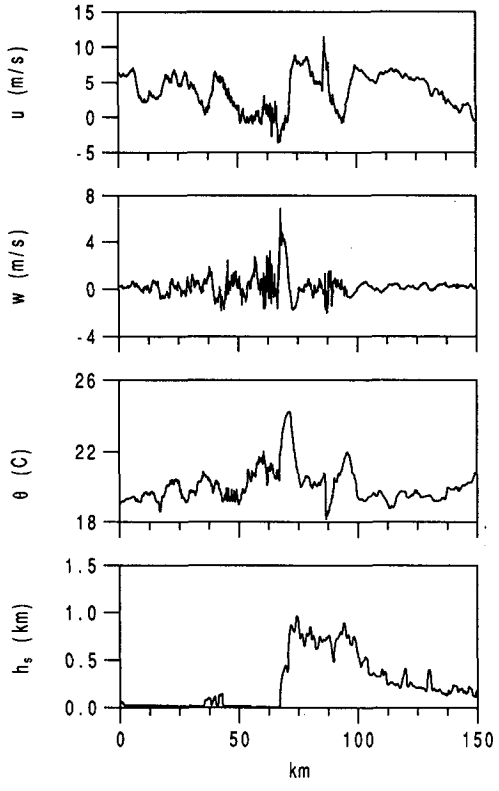

FIG. 2. Detrended observed u, w, and θ at the 3.3-km level on 6 March and the topography height. The mean flow is northeasterly and directed toward the left.

3. Observed wave momentum flux

The momentum flux due to wave-scale motions on 6 and 25 March for each flight leg is calculated by averaging the product between the bandpass-filtered horizontal and vertical velocities as

$$\overline{\tilde{u}\tilde{w}}(z) = \frac{1}{N}\sum_{i=1}^{N} \tilde{u}_i(z)\tilde{w}_i(z) \tag{2}$$

$$\overline{\tilde{v}\tilde{w}}(z) = \frac{1}{N}\sum_{i=1}^{N} \tilde{v}_i(z)\tilde{w}_i(z), \tag{3}$$

where $\tilde{}$ represents the wave-scale (bandpass-filtered) disturbance, N is the number of points in the averaging region, and the subscript i denotes the position along the flight path. The averaging is performed for a 80-km section of the flight track above the coastal range where the wave activity is significant. The average momentum flux is somewhat sensitive to the averaging length. This sensitivity may indicate sampling problems as discussed by Lumley and Panofsky (1964), Wyngaard (1972), and Lenschow and Stankov (1986). However, wave-scale motions and associated momentum fluxes observed in each flight leg appear to be stationary and confined to a region directly over the mountain range. Consequently, sampling problems for the current study are more related to defining the horizontal length scale of the wave activity than obtaining ensemble averages of random signals.

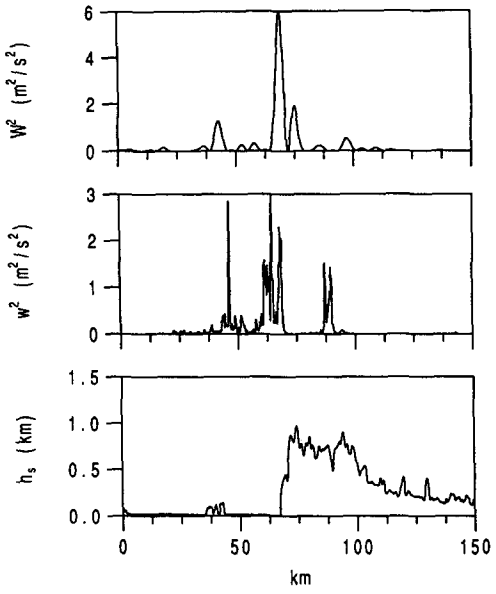

FIG. 3. Vertical velocity variances of the 10–80-km bandpass-filtered data (top) and the 1-km high-pass-filtered data (middle) observed on 6 March at the 3.3-km level.

The wave-scale momentum flux vector on the two days is generally directed in the opposite direction of the surface wind (Fig. 4a), as expected from linear gravity waves induced by terrain. Only on 6 March at higher levels does the direction of wave-scale momentum flux rotate away from this direction and by an angle of about 45 deg.

For comparison with the wave momentum flux formulations in section 6, we compute the *wave momentum flux* $\tilde{M}_w$ as the component of bandpass momentum flux in the opposite direction of the surface wind $\mathbf{V}_0$ as

$$\tilde{M}_w \equiv -\frac{\tilde{M}\cdot \mathbf{V}_0}{|\mathbf{V}_0|}, \qquad (4)$$

where $\tilde{M}$ is the vector of wave-scale momentum flux $(\tilde{u}\tilde{w}, \tilde{v}\tilde{w})$ calculated from (2–3) and $\tilde{M}\cdot \mathbf{V}_0$ represents the scalar product of the flux vector $\tilde{M}$ and the surface wind $\mathbf{V}_0$. This wave momentum flux decreases with increasing height on 6 March, consistent with the expected occurrence of wave breaking on this day (Fig. 5, open circles). Without wave breaking, conservation of wave stress implies that the wave momentum flux should increase with height due to the decrease of atmospheric density with height. The wave momentum flux is about 2.8 m^2 s^{-2} at the 2.4-km level and decreases to about 0.5 m^2 s^{-2} at the 4,5-km level (Fig. 5). This vertical decrease of the wave momentum flux implies deceleration of the mean wind component parallel to the surface wind at a rate of about 9×10^{-4} m s^{-2}. This deceleration rate is comparable to the magnitude of the Coriolis term. Thus, wave drag appears to be important in the evolution of the low-level flow over the coastal range on this day.

In contrast, the wave momentum flux generally increases with increasing height on 25 March (Fig. 6, open circles). The magnitude of this increase of wave momentum flux with height is predicted by conservation of wave stress (section 6).

4. Wave equation

In section 6, we will compare the observed wave momentum flux with that predicted by formulations for linear gravity waves and wave breaking. The following two sections will develop these formulations by combining the nonlinear lower boundary condition of Smith (1977) with wave stress supersaturation theory of Lindzen (1988) after generalizing the wave-stress supersaturation theory for height-dependent mean flow.

A sinusoidal topography is considered, even though the actual coastal range is asymmetric with the southwestern slope steeper than the northeastern slope. Previous studies (Smith 1977; Lilly and Klemp 1979) show that such asymmetry of the topography increases the maximum slope of the streamlines. However, we are concerned with a simple formulation of wave drag to be used in coarse-resolution numerical models where the consideration of detailed shape of topography is not possible.

Although portions of the following derivation are completely analogous to Smith (1977) or Lindzen

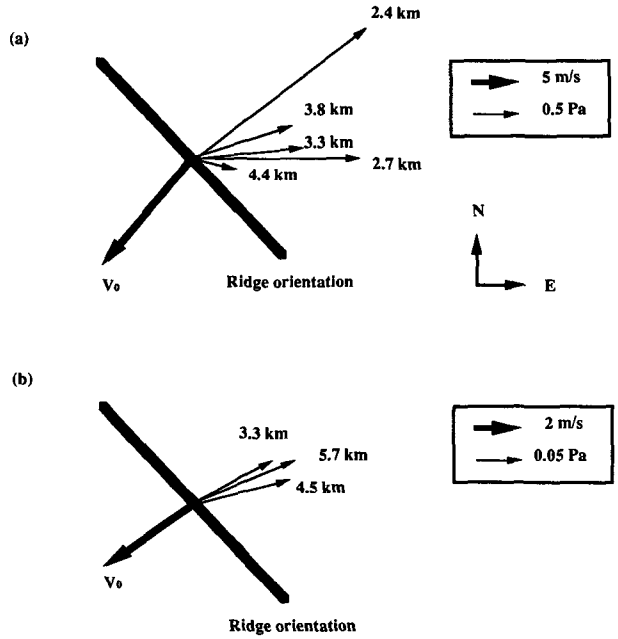

FIG. 4. Observed wave-scale momentum flux vectors (thin arrows) and surface wind $\mathbf{V}_0$ (thick arrows) for (a) 6 March and (b) 25 March.

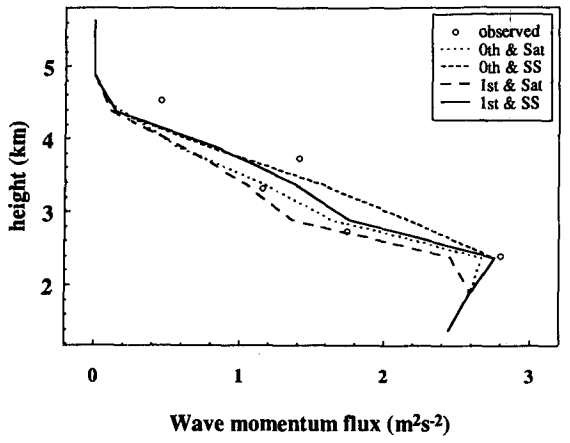

FIG. 5. Observed momentum flux from the 10–80-km bandpass-filtered variables (open circles) and model-estimated wave momentum flux (lines) on 6 March 1982 with the zero-order (0th) and first-order (1st) lower boundary conditions and wave-stress saturation (SS) and supersaturation (SS) conditions.

(1988), they are included here in abbreviated form for continuity of the derivation. The reader not interested in the derivation of the wave stress formulation may advance to section 6. The disturbance field of a streamline for a linear, stationary gravity wave in a steady, incompressible, hydrostatic flow can be expressed by Long's equation (Long 1953)

$$\nabla^2\delta + l^2\delta = 0, \tag{5}$$

where ∇^2 is a two-dimensional Laplacian operator in the $x - z$ plane, $\delta \equiv z - z_0$ is the vertical displacement of the streamline height from its undisturbed upstream value z_0, and l is the Scorer parameter, or vertical wavenumber, defined as

$$l^2 \equiv -\frac{1}{U^2}\frac{g}{\rho}\frac{d\rho}{dz_0} \equiv \frac{N^2}{U^2}. \tag{6}$$

Assuming that the horizontal wavelength of the motion is much larger than the vertical wave length, which can be justified for the cases considered in this study, the terms containing second-order derivatives in the horizontal are neglected, while those containing second-order derivatives in the vertical are retained. Then, expanding the Laplacian operator, (5) can be approximated as

$$\frac{\partial^2\delta}{\partial z^2} + l^2\delta = 0. \tag{7}$$

Assuming further that surface topography is the only source of gravity waves, the radiation boundary condition is applied at the top of the domain. At the bottom of the domain, a kinematic boundary condition

$$\delta(x, \eta(x)) = \eta(x) \tag{8}$$

is imposed, where $\eta(x)$ is the height of the ground topography and $\delta(x, \eta(x))$ is the vertical displacement of a streamline at the ground level. In (8), the amplitude of terrain-induced gravity waves is assumed equal to the height of the ground topography.

For simplicity, we assume a monochromatic sinusoidal topography with an amplitude η_0 defined as

$$\eta(x) = \eta_0 \cos(kx), \tag{9}$$

where k is the horizontal wavenumber. In the presence of vertical shear and vertically varying stratification, the solution for $\delta(x, z)$ in (7) with the first-order approximation of the lower boundary condition (9) and the WKB approximation can be written as (Smith 1977)

$$\delta(x, z) = h(z)\left[\cos(kx + \phi) + \frac{h_0 l_0}{2}\sin(2kx + \phi)\right], \tag{10}$$

where $\phi(z) \equiv \int^z l(z')dz'$ is the vertical wave phase, $h(z)$ is the amplitude of the streamline disturbances at height z, l_0 is the Scorer parameter at the ground, and h_0 is the amplitude of the vertical displacement of the streamline at the ground assumed equal to the amplitude of the surface topography η_0.

The amplitude of the vertical displacement of the streamline height, $h(z)$, can be estimated from conservation of wave stress (Eliassen and Palm 1960) or conservation of wave action (Smith 1977) for linear internal gravity waves. The relationship between the mean flow profile and the amplitude of streamline disturbances for linear monochromatic gravity waves can be expressed as (Smith 1977)

$$\rho(z)U(z)N(z)k\overline{\delta^2}(z) = \text{const}, \tag{11}$$

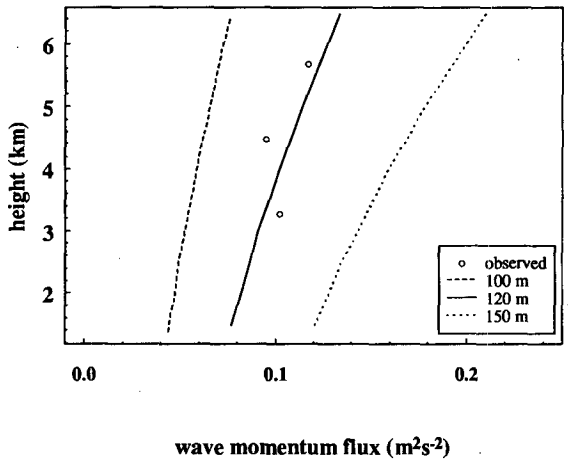

FIG. 6. Observed momentum flux from 10–80-km bandpass variables (open circles) and model-estimated wave momentum fluxes for different effective mountain heights (lines).

where $\overline{\delta^2}(z)$ is the mean-square amplitude of the gravity wave at height z and $\bar{(\ )}$ denotes horizontal averaging over one wavelength. The mean-square amplitude $\delta^2(z)$ is obtained from (10) as

$$\overline{\delta^2}(z) = \frac{h^2(z)}{2}\left[1 + \frac{(h_0 l_0)^2}{4}\right]. \quad (12)$$

Combining (11) and (12), the ratio of the amplitude of the streamline displacement at height z above the ground to the amplitude at the ground level, $\gamma(z)$, becomes (Smith 1977)

$$\gamma(z) \equiv \frac{h(z)}{h_0} = \left(\frac{\rho_0 U_0 N_0}{\rho(z) U(z) N(z)}\right)^{1/2}, \quad (13)$$

where the subscript 0 denotes the value at the ground level. Relationship (13) indicates that internal gravity waves amplify during the vertical propagation due to decreasing density, wind speed, and stratification[1] of the mean flow with increasing height.

The average stress exerted by a gravity wave, $\tau_w(z)$, is calculated by

$$\tau_w(z) = -\rho(z)\overline{\tilde{u}\tilde{w}}(z) = -\frac{1}{L}\int_{-L/2}^{L/2} \rho(z)\tilde{u}(x, z)\tilde{w}(x, z)dx, \quad (14)$$

where L is the horizontal wavelength of the wave, and $\tilde{u}(x, z)$ and $\tilde{w}(x, z)$ are disturbance horizontal and vertical components of wind due to wave activity given as

$$\tilde{u} = -U\left[\frac{\partial \delta}{\partial z}\right](x, z) \quad (15a)$$

$$\tilde{w} = U\left[\frac{\partial \delta}{\partial x}\right](x, z), \quad (15b)$$

where U is the mean wind speed and $\delta(x, z)$ is again the vertical displacement of the streamline (10). Substituting $\tilde{u}$ (15a) and $\tilde{w}$ (15b) into (14) and using (12), the average wave stress for the gravity wave solution with first-order lower boundary condition becomes

$$\tau_w(z) \approx \frac{k}{2}\rho(z)U(z)N(z)[h_0\gamma(z)]^2\left[1 + \frac{(h_0 l_0)^2}{4}\right]. \quad (16)$$

The wave stress at the ground surface is obtained from (16) by using ρ, U, and N at the ground level with $\gamma = 1$. In (16), the influence of the height of surface topography enters through the wave amplitude at the ground surface h_0 and through the ratio $\gamma(z)$. Recalling that the above development is based on the conservation of wave stress, (16) becomes invalid at the level where wave breaking occurs, which is the subject of the next section.

5. Wave breaking and wave-stress supersaturation

As the amplitude of a gravity wave increases with height, the flow modified by the wave activity can become locally unstable, thus limiting the maximum growth of wave amplitude (saturation hypothesis; Lindzen 1981). The major mechanism of wave breaking can be either shear-driven Kelvin–Helmholtz instability or convective instability. Thorpe (1973) observed in laboratory experiments that disturbances begin to grow when the gradient Richardson number of the mean flow decreases below 0.25. Klemp and Lilly (1978) adjusted the local flow with respect to the Kelvin–Helmholtz instability criterion and successfully approximated the observed wave disturbance. On the other hand, Smith (1977) and Lindzen (1981) have argued that the growth rate of perturbations by convective instability is much faster than that by Kelvin–Helmholtz instability. As a possible result of this faster growth rate, Delisi and Orlanski (1975) observe well-defined convection in wave breaking regions in rotating tank experiments. Pitts and Lyons (1990) also find convective overturning in numerical simulations of stratified flow over topography. In the present study, the convective instability criterion will be used to derive wave-breaking conditions.

The saturation hypothesis (Lindzen 1981) assumes that the maximum slope of a wave streamline will be limited by the onset of convective instability. Parameterizations of gravity wave drag by Palmer et al. (1986) and McFarlane (1987) assume that the amplitude of a saturated gravity wave is determined by marginal hydrodynamic stability in wave breaking regions. On the other hand, Smith (1977) and Lindzen (1988) suggest that breaking gravity waves may maintain some degree of convective instability in the wave breaking region.

With supersaturation theory (Lindzen 1988), the perturbation of a streamline is constrained by the relationship

$$\left(\frac{\partial \delta}{\partial z}\right)_{\max}(z) \leq 1 + S(z), \quad (17)$$

where $(\partial\delta/\partial z)_{\max}(z)$ is the maximum value of the quantity $(\partial\delta/\partial z)(x, z)$ at a given level and $S(z)$ is the degree of supersaturation at level z. When $S(z) > 0$, (17) implies reversal of the slope of the streamline so that some degree of convective instability is maintained in the wave breaking region. When $S(z) = 0$, (17) reduces to the expression for the usual wave-stress saturation condition with respect to the convective instability.

[1] The amplitude of a gravity wave increases with decreasing stratification in the vertical. However, wave steepening increases for a given value of wave amplitude with increasing stratification with height as shown by (35–36) in section 5.

Lindzen (1988) estimates the degree of supersaturation $S(z)$ by considering the balance between the reduction of the wave amplitude due to wave breaking and the growth of the wave amplitude due to vertical variation of the mean flow. Lindzen (1988) also assumes a balance between the rate at which the wave loses its energy to convective instability and the rate at which the wave motion transports energy into the wave-breaking region. In the following development, we generalize the wave-stress supersaturation theory of Lindzen (1988) to include vertically varying mean flows for comparison with atmospheric data. Then the supersaturated wave stress will be estimated for the wave solution with the first-order lower boundary condition. The cases for the zero-order lower boundary condition or wave stress saturation condition can be recovered from this result by neglecting the appropriate terms in the final result.

The net percentage change of the mean-square amplitude of the wave due to wave breaking in a given layer, $F(\alpha)$, can be obtained as a function of the *half-width of the wave breaking region* α analogous to Lindzen [1988; his Eq. (13)]

$$F(\alpha) = f(\alpha)g(\alpha). \tag{18}$$

In (18) the reduction factor $f(\alpha)$ is defined as the ratio of the mean-square amplitude with wave breaking to that without wave breaking. The amplification factor $g(\alpha)$ denotes the increase of the mean-square amplitude across the layer due to the height dependence of the mean flow in the layer in the absence of wave breaking.

Assuming complete flattening[2] of the streamline by the action of wave breaking alone, Lindzen [1988; his Eq. (8)] estimates the reduction factor $f(\alpha)$ for a sinusoidal wave to be

$$f(\alpha) = \frac{\pi - \alpha + 0.5 \sin(2\alpha)}{\pi}. \tag{19}$$

The amplification factor[3] $g(\alpha)$ for the convectively unstable layer of depth D is obtained from (12)–(13) as

$$g(\alpha) \equiv \frac{\overline{\delta^2}(z + D)}{\overline{\delta^2}(z)} = \frac{\gamma^2(z + D)}{\gamma^2(z)}, \tag{20}$$

where $\overline{\delta^2}$ and γ again are the mean-square amplitude (12) and the normalized amplitude (13) of the gravity wave, respectively.

The amplification factor $g(\alpha)$ depends on the vertical variations of the atmospheric density, mean wind speed, and stratification. To make an analogy to the isothermal atmosphere with constant wind speed where $g(\alpha)$ depends only on the vertical variation of the atmospheric density, an *equivalent scale height* H, defined from local variation of the mean flow, is introduced. The amplification factor (20) can then be rewritten in terms of an equivalent scale height as

$$g(\alpha) = e^{D/H}. \tag{21}$$

The argument of the exponent in (21) is in terms of D/H instead of $D/2H$, which appeared in Lindzen (1988), because the growth of the mean-square amplitude is of concern here. Accordingly, a height-dependent equivalent scale height H can be determined from (20) and (21) as

$$H = \frac{D}{\ln[\gamma^2(z + D)/\gamma^2(z)]}. \tag{22}$$

For the case of an isothermal atmosphere with constant wind speed, expression (22) for the equivalent scale height reduces to the usual definition of the scale height for an isothermal atmosphere (RT/g). If $\gamma^2(z + D) < \gamma^2(z)$, H becomes negative in which case wave breaking does not occur and wave stress is conserved. Using the equivalent scale height (22), we can now follow the general procedure presented by Lindzen (1988).

The depth of the convectively unstable region D can be estimated from the shape of the streamline disturbance $\delta(x, z)$ and the half-width of the wave breaking region α. Then the depth D is the difference of the height of the streamline $\delta(x, z)$ between the points where $kx + \phi = 3\pi/2 - \alpha$ and $kx + \phi = 3\pi/2 + \alpha$, respectively. Neglecting the first-order term in the expression for $\delta(x, z)$ in (10), this depth D then simplifies to

$$\begin{aligned} D &\approx \mu h(z)\left[\cos\left(\frac{3}{2}\pi + \alpha\right) - \cos\left(\frac{3}{2}\pi - \alpha\right)\right] \\ &= 2\mu h(z) \sin\alpha, \end{aligned} \tag{23}$$

where $h(z)$ is again the amplitude of the streamline disturbance at z and μ is a positive constant less than unity, which accounts for the reduction of the vertical propagation of the wave by convection as proposed by Lindzen (1988). Using the normalized wave amplitude (13), the depth of the convectively unstable region D in (23) can be rewritten as

$$D = 2\mu h(z) \sin\alpha = 2\mu h_0 \gamma(z) \sin\alpha. \tag{24}$$

The constant μ is estimated by equating the convective time scale with the time scale for the vertical propa-

[2] The streamlines in the wave breaking regions will not be completely flat. Dunkerton (1989) assumes linear slope, while Lindzen (1988) does not introduce any particular shape of the streamline. However, the amplification factor $g(\alpha)$ in (18) is equivalent to assuming nonzero slope of the streamline when computing the mean-square amplitude.

[3] In Lindzen (1988), the amplification factor [his Eq. (12)] is calculated for the amplitude, while the flattening $f(\alpha)$ [or the reduction factor; his Eq. (9)] is calculated for the mean-square amplitude. Hence, the current derivation is more consistent.

gation of the wave energy across the convectively unstable layer (Lindzen 1988) as

$$\mu \approx \frac{U}{N}\left(\frac{\sqrt{2}}{6\pi}\frac{k}{H}\right)^{1/2}\frac{H}{h_0\gamma} = \left(\frac{\sqrt{2}}{3}\frac{H}{L}\right)^{1/2}\frac{1}{h_0\gamma l}. \quad (25)$$

Assume that the wave breaking occurs in a region that is narrow compared to the horizontal wavelength ($\alpha \ll \pi$) and that the depth of the convectively unstable layer is small compared to the equivalent scale height ($D \ll H$). Then the net percentage change of the mean-square amplitude $F(\alpha)$ and the depth of convectively unstable layer D can be approximated by expanding $\sin\alpha$, $\cos\alpha$, and $e^{D/H}$ in (19), (24), and (21) in terms of small values of α and D/H in which case

$$F(\alpha) \approx \left(1 - \frac{2}{3\pi}\alpha^3\right)\left(1 + \frac{D}{H}\right) \approx 1 + \frac{D}{H} - \frac{2}{3\pi}\alpha^3, \quad (26)$$

$$D = 2\mu h_0\gamma \sin\alpha \approx 2\mu h_0\gamma(z)\left(\alpha - \frac{\alpha^3}{6}\right). \quad (27)$$

At an equilibrium state, the reduction factor $f(\alpha)$ balances the amplification factor $g(\alpha)$ for the mean-square amplitude in the wave breaking region so that

$$F(\alpha_e) = 1, \quad (28)$$

where α_e denotes the half-width of the wave breaking region at the equilibrium state. This equilibrium half-width α_e can then be estimated from (26)–(28) as

$$\alpha_e = \left(\frac{6\mu h_0\gamma}{\mu h_0\gamma + 2H/\pi}\right)^{1/2}, \quad (29)$$

where μ is given by (25).

Now $(\partial\delta/\partial z)_{\max}$ [or $\tilde{A}$ in Lindzen (1988)] for a breaking wave can be obtained from the geometric argument of Lindzen (1988; see his Fig. 1) as

$$\left(\frac{\partial\delta}{\partial z}\right)_{\max} = \frac{1}{\cos\alpha_e}. \quad (30)$$

Expanding $\cos\alpha_e$ for small α_e in (30) and substituting μ from (25) into (29), an approximate expression for $(\partial\delta/\partial z)_{\max}$ is obtained:

$$\left(\frac{\partial\delta}{\partial z}\right)_{\max} \approx 1 + \frac{3}{2}\frac{(\pi/l)(\sqrt{2}H/3L)^{1/2}}{(\pi/l)(H/3\sqrt{2}L)^{1/2} + H}. \quad (31)$$

The degree of supersaturation, $S(z) \equiv (\partial\delta/\partial z)_{\max} - 1$, is then obtained from (31) as

$$S(z) = \frac{3}{2}\frac{(\pi/l)(\sqrt{2}H/3L)^{1/2}}{(\pi/l)(H/3\sqrt{2}L)^{1/2} + H}. \quad (32)$$

The first term in the denominator on the right-hand side of (32), which is absent in Lindzen's result, comes from the new expression for the depth of the convectively unstable region D in (23). This term is thought to be smaller than the equivalent scale height H. When this term is neglected, the degree of supersaturation estimated in the present study is simply a factor of $\sqrt{2}$ larger than that estimated by Lindzen (1988). This difference is due to the revised estimate of the amplification factor $g(\alpha)$ in (21).

Having estimated the degree of supersaturation, we proceed to calculate the corresponding supersaturated wave stress. From the wave solution with first-order lower boundary condition (10), the quantity $\partial\delta/\partial z$ becomes

$$\frac{\partial\delta}{\partial z}(x, z) = h(z)l(z) \times\left[-\sin(kx + \phi) + \frac{h_0 l_0}{2}\cos(2kx + \phi)\right]. \quad (33)$$

Expressing the wave amplitude $h(z)$ in terms of the normalized wave amplitude (13), (33) becomes (Smith 1977)

$$\frac{\partial\delta}{\partial z}(x, z) = h_0 l_0\gamma' \times\left[-\sin(kx + \phi) + \frac{h_0 l_0}{2}\cos(2kx + \phi)\right], \quad (34)$$

where γ' represents the vertical variation of the mean flow defined as

$$\gamma' \equiv \frac{\gamma(z)l(z)}{l_0} = \left(\frac{N(z)}{N_0}\right)^{1/2}\left(\frac{U(z)}{U_0}\right)^{-3/2}\left(\frac{\rho(z)}{\rho_0}\right)^{-1/2}. \quad (35)$$

For the wave solution with zero-order lower boundary condition, the second term in the square bracket of (34) is omitted.

The maximum value of $\partial\delta/\partial z$ at height z occurs where $\sin(kx + \phi) = -1$ and is obtained from (34) as

$$\left(\frac{\partial\delta}{\partial z}\right)_{\max}(z) = h_0 l_0\gamma'(z)\left[1 - \frac{h_0 l_0}{2}\cos\phi\right]. \quad (36)$$

Relationships (35)–(36) imply that for a given wave amplitude, $(\partial\delta/\partial z)_{\max}$ increases as ρ and U decrease with height and N increases with height. Using (36), the wave-breaking condition (17) can be expressed in terms of the vertical profile of the mean flow and the surface wave amplitude as

$$h_0 l_0\gamma'(z)\left[1 - \frac{h_0 l_0}{2}\cos\phi\right] \leq 1 + S(z). \quad (37)$$

If the inequality (37) is satisfied for an arbitrary model layer, the wave stress is conserved and the wave amplitude $h(z)$ varies across the layer according to (13). If the inequality (37) is not satisfied, then wave breaking occurs and the incident wave stress (16) at the bottom of the layer is reduced to the supersaturated value at the top of the layer.

The supersaturated wave stress can be obtained from (16) as

$$\tau_w(z) \approx \frac{1}{2} k\rho(z)U(z)N(z)[h_m\gamma(z)]^2\left[1 + \frac{(h_m l_0)^2}{4}\right], \quad (38)$$

where h_m is the surface wave amplitude resulting from imposing the supersaturation condition corresponding to equality in (37) so that

$$h_m l_0 \gamma'(z)\left[1 - \frac{h_m l_0}{2}\cos\phi\right] = 1 + S(z). \quad (39)$$

Solving (39) for the positive real value of $h_m l_0$, h_m is obtained as

$$h_m = \frac{1 + S}{l_0\gamma'} \quad \cos\phi = 0 \quad (40a)$$

$$h_m = \frac{1}{l_0\cos\phi}\left[1 - \left(1 - \frac{2(1+S)}{\gamma'}\cos\phi\right)^{1/2}\right]$$

$$\cos\phi < 0 \quad (40b)$$

$$h_m = \frac{1}{l_0\cos\phi}\left[1 + \left(1 - \frac{2(1+S)}{\gamma'}\cos\phi\right)^{1/2}\right]$$

$$\cos\phi > 0. \quad (40c)$$

A real solution for $h_m l_0$ from (39) exists only for $\cos\phi \leq \gamma'/2(1+S)$. When $\cos\phi > \gamma'/2(1+S)$, the contribution from the first-order lower boundary condition suppresses the wave steepening enough to prevent wave breaking, and wave stress is conserved. Solutions for the zero-order lower boundary condition are also given by (40a).

In model calculations, the wave stress is computed from layer to layer beginning at the ground surface. When wave breaking does not occur, the wave stress is constant across the layer. When wave breaking occurs, the supersaturated wave stress is computed from (38) with the appropriate value of h_m from (40a–c). To replace the supersaturation condition with the saturation condition, S in (40a–c) is set to zero. Dropping the second term in the square brackets of (38) and using (40a) for h_m, the supersaturated wave stress for zero-order lower boundary condition is recovered. Finally, the deceleration of the mean-flow component parallel to the low-level wind is obtained as

$$\left(\frac{\partial U}{\partial t}\right)_w = \frac{1}{\rho}\frac{\partial \tau_w}{\partial z}. \quad (41)$$

The wave momentum flux profiles computed from this model for 6 and 25 March ALPEX are compared with the observed wave momentum flux in the next section.

6. Modeled wave momentum flux for ALPEX

The wave momentum fluxes are now calculated from the wave momentum flux models with zero- and first-order lower boundary conditions and wave stress saturation and supersaturation conditions as described in the previous section. The parallel wind component and potential temperature profiles observed on 6 and 25 March in ALPEX (Figs. 1b,d) are used as the upstream conditions for model calculations. Based on the peak of the *variance spectra* of the Haar transform of V_p (Gamage 1990; Mahrt 1991), the horizontal wavelength is taken as 60 km, which agrees with the approximate width of the ridge. For the computation of the surface stress, the mountain height η_0 in (9) is estimated in terms of an effective mountain height taken as 500 and 120 m for 6 and 25 March, respectively, as will be discussed in the next section.

For 6 March, the modeled wave momentum flux decreases with height below the critical level as a result of wave breaking (Fig. 5). This decrease with height is also observed from the actual aircraft data (Fig. 5). However, the magnitude of the observed momentum flux increases substantially as the record is shortened to include only the inner region of strongest fluxes. Therefore, the observations cannot be used to discriminate between the flux magnitudes of the different models. The direct observational evidence of wave-induced convection shown in section 8 will be stronger support for the hypothesis of wave-stress supersaturation. The divergence of the modeled wave momentum flux corresponds to mean flow deceleration in the layer between 2.5 to 5 km at a rate of 10^{-3} m s^{-2}. Acting alone, this estimated wave-stress divergence would decelerate an inflow of 20 m s^{-1} by approximately 3 m s^{-1} over the 60-km-wide region.

On 6 March, the model predicts the maximum degree of supersaturation to be 18% at 3 km above sea level (Fig. 7). The wave momentum flux estimated with the supersaturation condition is about 35% larger than that estimated with the wave-stress saturation condition at the 3-km level (Fig. 5). For 25 March, wave breaking is not predicted by any combination of lower boundary conditions and wave-breaking conditions. The calculated wave momentum flux increases with increasing height for all models, in agreement with observations (Fig. 6, solid line).

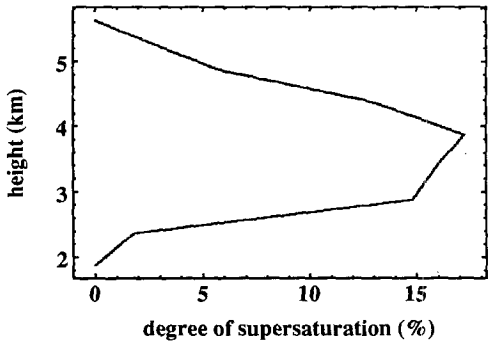

FIG. 7 The degree of supersaturation estimated for 6 March.

Although neglected in this study, the steeper lee side of the coastal range is expected to enhance wave steepening and reduce the wave stress at the wave breaking levels (Smith 1977; Lilly and Klemp 1979). However, assessment of such influences from the data seems tenuous within the suspected accuracy of the fluxes.

As an additional complication, wave reflection at the critical level or wave breaking level can cause a *high-drag* state (Peltier and Clark 1979), which interferes with the waves below the wave breaking level. The difference of the wave phase between the ground surface and the first wave breaking level estimated for 6 March corresponds to the low-drag state. However, the continuous occurrence of wave breaking between 2.5 km and 5 km on this day makes it difficult to find the exact level of wave reflection, if one exists.

7. Effective mountain height

Calculation of the wave stress at the ground level requires estimation of the effective mountain height. The actual displacement of the streamline near the ground surface is influenced by terrain-induced disturbances such as the blocking of low-level flow (Klemp and Lilly 1978; Pierrehumbert and Wyman 1986), the development of turbulent boundary layer (Pitts and Lyons 1990), and the formation of stagnant cold-air pools in topographic depressions. To take into account these effects, Palmer et al. (1986) limit the value of wave amplitude at the ground level to 400 m or less.

Based on two-dimensional model results, Stern and Pierrehumbert (1988) propose the effective mountain height η_e to be

$$\eta_e = \min\left[\eta_0, c\frac{U_0}{N_0}\right], \qquad (42)$$

where η_0 in this equation denotes the actual amplitude of the surface topography and c is a constant estimated to be 0.4–0.8 in their study.

We estimate the effective mountain height η_e by equating the model-estimated wave stress at ground level with the observed wave stress below the model-estimated wave breaking level, since wave stress is conserved below this level. Effective mountain heights of 500 m and 120 m appear to yield the best agreement between the observed and model-estimated fluxes for 6 and 25 March, respectively, although uncertainties in the observed values are large. Examples of the estimated wave momentum flux with various effective mountain heights are shown in Fig. 6 for 25 March. On this day the observed flux profile is simple and the model predicts no wave breaking. Using the above values of η_e and substituting the observed upstream wind and stratification into (42), the coefficient c in (42) is predicted to be, perhaps coincidentally, 0.32 for both days.

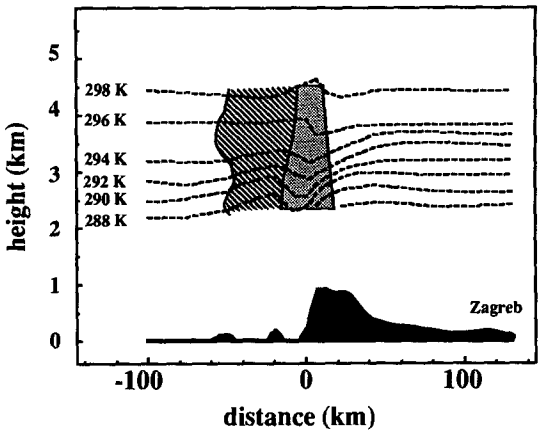

FIG. 8. A schematic diagram of the isentropes (after Smith 1987) and the regions of downward (shaded with lines) and upward (shaded with dots) turbulent heat flux observed on 6 March.

8. Upward turbulent heat flux in the wave breaking region

Comparison of the wave momentum flux estimated from the linear gravity wave models in the previous section suggests that the difference between the wave momentum flux predicted by wave-stress saturation and supersaturation conditions can be locally significant. However, direct observational verification of wave-stress supersaturation in the atmosphere has not been previously established.

One indication of wave-stress supersaturation and convective instability is upward turbulent heat flux. Turbulent heat fluxes calculated for each flight level on 6 March show a well-defined region of upward turbulent heat flux over the upstream edge of the coastal range (Fig. 8) located approximately where maximum wave steepening is expected.[4] The width of the upward turbulent heat flux region is approximately 10–20 km, depending on the altitude.

The occurrence of convectively driven turbulence can be seen from the horizontal variations of vertical velocity and potential temperature in the composite of eddy structures sampled from the upward heat flux region (Fig. 9). The 800-m-wide samples are centered at the positive peaks of the Haar wavelet transform of vertical velocity, which is used to detect concentrated eddy-scale gradients (Mahrt 1991). The selected samples represent about 80% of the total record length in the upward heat flux region, so that most of the record is represented. Similar structures with a factor of 2–3 smaller amplitudes occurred at the 3.7- and 4.4-km levels. In the composited structure, temperature and vertical velocity are almost exactly in phase (Fig. 9),

[4] The upward turbulent heat flux shown in Fig. 10 occurs approximately in the cloud-free region reported by Smith (1987) and is thus not due to latent heating.

which corresponds to well-organized convection and efficient upward heat flux. This convection is consistent with wave-stress supersaturation with respect to convective instability.

The estimated magnitude of turbulent heat flux generally decreases with height and varies with the cutoff wavelength for the high-pass filter. The upward heat flux at the 3.3-km level reaches a maximum for a 1-km filter cutoff wavelength (Fig. 11). Therefore, motions smaller than 1 km are regarded as turbulence-scale disturbances. The vertical profile of the heat flux calculated from 500-m high-pass–filtered variables is also presented for comparison (Fig. 10).

We now attempt to formulate the upward turbulent heat flux in the wave-breaking region using a flux-gradient relationship and the wave-stress supersaturation condition. The purpose of this formulation is to document the plausibility of the wave-stress supersaturation condition for wave breaking rather than to provide a practical tool for modeling.

The upward turbulent heat flux in a wave breaking region will be estimated by assuming a relationship between the turbulent flux and the local wave-modified gradient of the mean flow so that

$$\overline{w'\theta'} = -K\frac{\partial\theta}{\partial z}, \tag{43}$$

where K is the eddy diffusivity for heat and θ is the total potential temperature modified by wave activity. When the wave stress is supersaturated, $\partial\theta/\partial z$ in the wave breaking region is estimated by

$$\frac{\partial\theta}{\partial z} \approx \frac{\partial\Theta}{\partial z}\left[1 - \left(\frac{\partial\delta}{\partial z}\right)_{\max}\right] = -S\frac{\partial\Theta}{\partial z}, \tag{44}$$

where Θ is the mean potential temperature (not modified by wave activity) and S is the degree of supersaturation given by (32). In (44), nonzero supersaturation (positive S) corresponds to convective instability. With stronger stratification, wave breaking leads to greater convective instability.

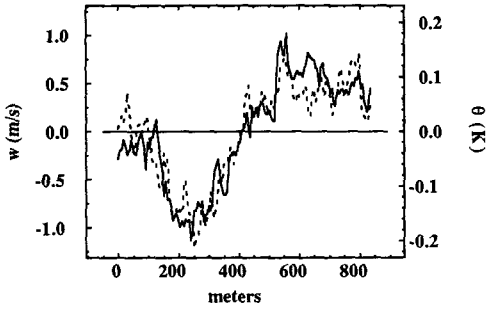

FIG. 9. The composite of w (dashed line) and θ (solid line) from sampled events in the upward turbulent heat flux region at the 3.3-km level on 6 March.

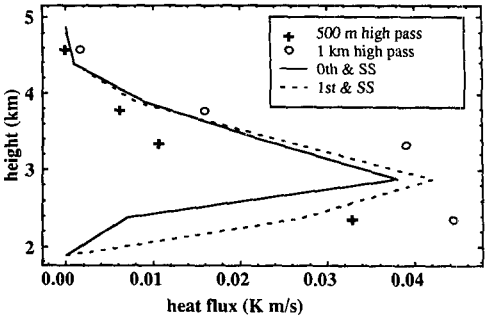

FIG. 10. The upward turbulent heat flux from high-pass–filtered variables with cutoff wavelengths at 500 m (cross) and 1 km (open circles) on 6 March and the model-predicted flux profiles (51).

The eddy diffusivity in the wave breaking region may be approximated as

$$K \approx l_w^2\left|\frac{dV}{dz}\right|, \tag{45}$$

where l_w is the turbulent length scale for heat transfer and V is the wind speed modified by wave activity. In the wave breaking region, the turbulent length scale l_w is presumably restricted by the depth of the wave breaking region D given by (27).

To estimate the wind shear in the wave breaking region, we estimate the minimum wind speed u_c due to the maximum modification of the flow by gravity waves as

$$u_c \approx U\left[1 - \left(\frac{\partial\delta}{\partial z}\right)_{\max}\right] = -SU, \tag{46}$$

where U is the unmodified mean wind speed in the direction of the surface wind. Then the maximum dif-

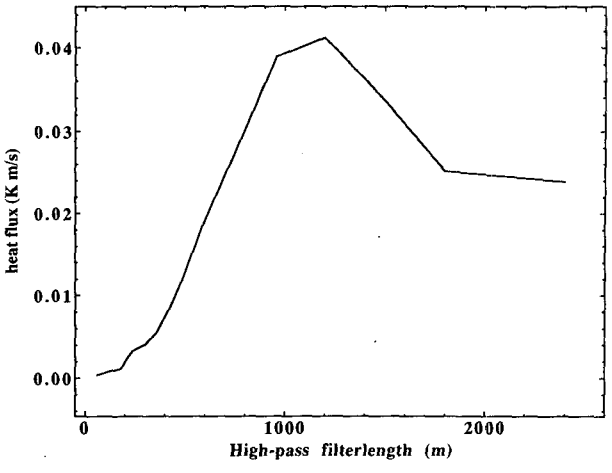

FIG. 11. The turbulent heat flux for different high-pass filter lengths in the upward turbulent heat flux region at the 3.3-km level on 6 March.

ference of the wave-modified wind speed ΔV across a depth comparable to the amplitude of the wave streamline displacement is approximated as

$$\Delta V \approx U - u_c = (1 + S)U. \tag{47}$$

The corresponding shear of the wave-modified flow in the wave breaking region can be obtained from (47) as

$$\left|\frac{dV}{dz}\right| \approx \frac{\Delta V}{h(z)} = \frac{(1 + S)U}{h(z)}, \tag{48}$$

where $h(z)$ is, again, the amplitude of the vertical displacement of the streamline. We have assumed that the background mean shear is small compared to the wave-induced shear.

Assuming the mixing length to be proportional to the depth of wave breaking region and using the estimated wind shear (48), the eddy diffusivity in the wave breaking region may be approximated as

$$K = C_K D^2 \frac{(1 + S)U}{h(z)}, \tag{49}$$

where C_K is a constant with expected magnitude less or equal to 1. From (25), (27), and (29), D^2 can be estimated to be

$$D^2 = a\left(\frac{H}{L}\right)^{1/2} k\left(\frac{U}{N}\right)^3, \tag{50}$$

where $a \equiv (2^{3/2}/3)^{1/2} \approx 0.97$.

Finally, the turbulent heat flux in the wave breaking region can be estimated from (43)–(44) and (49)–(50), together with the degree of supersaturation S from (32) to be

$$\overline{w'\theta'} \approx C_K D^2 \frac{(1 + S)U}{h(z)} S \frac{d\Theta}{dz}. \tag{51}$$

Using $C_K = 1$, the model-estimated upward turbulent heat flux decreases with increasing altitude similar to the observed fluxes (Fig. 10). The decrease of upward turbulent heat flux with height results mostly from the decrease of the depth of convection D with height. The comparison between model results and the observations also suggests that the constant C_K in (51) is order of unity.

A wide region of downward turbulent heat flux occurs at the back of the wave immediately downstream from the narrower region of upward turbulent heat flux (Fig. 8). The upward and downward heat flux approximately cancel each other when averaging over the entire record. The wave-scale heat flux is also small when averaged over the entire record at different levels. As a result, the total wave and turbulent heat flux and its influence on the mean stratification appear to be small for this day. Similar results are obtained by Delisi and Orlanski (1975) and Dunkerton (1989) from rotating tank experiments. In addition, the turbulent momentum flux is one or two orders of magnitude smaller than the wave momentum flux. Thus, the transport of momentum by gravity waves appears to be the primary vertical transport mechanism for the two flow cases studied here.

9. Conclusions

We have studied two distinctly different atmospheric flows over the coastal range of northern Yugoslavia with aircraft measurements collected during ALPEX. On 6 March, steepening and breaking of orographic gravity waves occur, and the wave momentum flux decreases with increasing height below the critical level. Deceleration of the wind component parallel to the surface wind due to this wave-stress divergence appears to be about 9×10^{-4} m s^{-2}, a value comparable to the magnitude of the Coriolis term in the momentum equations. On 25 March, low-level wave breaking does not occur and the wave momentum flux increases with height. On both days, the region of wave activity is 60–70 km wide, coinciding with the width of the underlying coastal range.

The wave momentum flux estimated from the linear gravity wave model agrees with the observed wave momentum flux on both days. The wave momentum flux with the first-order lower boundary condition is 20%–30% smaller than that with zero-order lower boundary condition. The generalized wave-stress supersaturation condition predicts 20%–40% more wave stress on 6 March compared to application of the wave-stress saturation condition. However, the difference between these models may not be significant compared to uncertainties of the flux computed from observations and uncertainties in model-input variables. The estimated effective mountain heights from the observations agree with the formulation suggested by Stern and Pierrehumbert (1988).

The region of observed upward turbulent heat flux on 6 March, 10–20 km wide, contains well-defined convective eddies on the turbulent scale. These eddies provide evidence for wave-stress supersaturation with respect to convective instability. The vertical profile of the observed upward turbulent heat flux can be approximated by a flux gradient relationship based on the mixing length and vertical shear derived from the generalized supersaturation theory. However, the net turbulent heat flux over the entire flight path appears to be small due to cancellation between the upward flux in the convectively unstable region and downward heat flux at the back of the wave. Therefore, the turbulent heat flux may not significantly influence the mean stratification at the wave-breaking level in agreement with the studies of Delisi and Orlanski (1975), Fritts and Dunkerton (1985), and Dunkerton (1989). The spatially averaged transport of heat by wave-scale motions and transport of momentum by turbulence also appear to be small compared to suspected sampling

problems. Therefore, vertical transport of momentum by gravity waves is the principal mechanism of vertical transport for both of the flow regimes studied here.

We neglected three-dimensionality of the ground topography, which could lead to overestimation of the wave momentum flux (Blumen and McGregor 1976). Nappo and Chimonas (1992) found that wave stress over an idealized three-dimensional topography is about half of that over two-dimensional topography with the same amplitude and width. However, the detailed influence of the three-dimensionality will depend upon the ratio between the along-ridge and cross-ridge length scales (Pierrehumbert and Wyman 1986). Application of the wave momentum flux formulation to numerical models must also recognize that subgrid-scale topography generally includes mountains with a variety of effective mountain heights and horizontal scales that vary according to the geographical location and grid size. Application of the gravity-wave momentum flux formulation to numerical models also requires compatibility with the formulation of the planetary-boundary layer (Pitts and Lyons 1990). Such application may include generation of critical levels in the stable boundary layer (Nappo and Chimonas 1991), which prevents propagation of gravity waves out of the boundary layer.

Acknowledgments. We gratefully acknowledge the comments of Tim Dunkerton and the reviewers and the computational assistance of Wayne Gibson. We also thank Ron Smith for providing the radiosonde data. This work is supported by Contract F19628-88-K-0001 from the Phillips Laboratory.

REFERENCES

Blumen, W., and C. D. McGregor, 1976: Wave drag by three-dimensional mountain lee-waves in nonplanar shear flow. *Tellus,* **28,** 287–298.

Brown, P. R. A., 1983: Aircraft measurements of mountain waves and their associated momentum flux over the British Isles. *Quart. J. Roy. Meteor. Soc.,* **109,** 849–865.

Chao, W. C., and M. R. Schoeberl, 1984: A note on the linear approximation of gravity wave saturation in the mesosphere. *J. Atmos. Sci.,* **41,** 1893–1898.

Delisi, D. P., and I. Orlanski, 1975: On the role of density jump in the reflection and breaking of internal gravity waves. *J. Fluid Mech.,* **69,** 445–464.

Drazin, P. G., 1961: On the steady flow of a fluid of variable density past an obstacle. *Tellus,* **13,** 239–251.

Dunkerton, T. J., 1989: Theory of internal gravity wave saturation. *Paleogeophysics,* **130,** 373–397.

Eliassen, A., and E. Palm, 1960: On the transfer of energy in stationary mountain waves. *Geophys. Publ.,* **22,** 1–23.

Fritts, D. C., and T. J. Dunkerton, 1985: Fluxes of heat and constituents due to convectively unstable gravity waves. *J. Atmos. Sci.,* **42,** 549–556.

Gamage, N., 1990: Modeling and analysis of geophysical turbulence: Use of optimal transforms and basis sets. Ph.D. thesis, Oregon State University, 135 pp.

Hoinka, K. P., 1985: Observation of the airflow over the Alps during a foehn event. *Quart. J. Roy. Meteor. Soc.,* **111,** 199–224.

Holton, J. R., 1982: The role of gravity wave induced drag and diffusion in the momentum budget of the mesosphere. *J. Atmos. Sci.,* **39,** 791–799.

Hunt, B. G., 1990: A simulation of the gravity wave characteristics and interactions in a diurnally varying model atmosphere. *J. Meteor. Soc. Japan,* **68,** 145–161.

Jasperson, W. H., G. D. Nastrom, and D. C. Fritts, 1990: Further study of terrain effects on the mesoscale spectrum of atmospheric motions. *J. Atmos. Sci.,* **47,** 979–987.

Klemp, J. B., and D. K. Lilly, 1978: Numerical simulation of hydrostatic mountain waves. *J. Atmos. Sci.,* **35,** 78–106.

Lenschow, D. H., and B. B. Stankov, 1986: Length scales in the convective boundary layer. *J. Atmos. Sci.,* **43,** 1198–1209.

Lilly, D. K., and J. B. Klemp, 1979: The effects of terrain shape on nonlinear hydrostatic mountain waves. *J. Fluid Mech.,* **95,** 241–261.

——, J. M. Nicholls, R. M. Chervin, P. J. Kennedy, and J. B. Klemp, 1982: Aircraft measurement of wave momentum flux over the Colorado Rocky Mountains. *Quart. J. Roy. Meteor. Soc.,* **108,** 625–642.

Lindzen, R. S., 1981: Turbulence and stress owing to gravity wave and tidal breakdown. *J. Geophys. Res.,* **86,** 9707–9714.

——, 1988: Supersaturation of vertically propagating internal gravity waves. *J. Atmos. Sci.,* **45,** 705–711.

Long, R. R., 1953: Some aspects of the flow of stratified fluids I. A theoretical investigation. *Tellus,* 42–58.

Lumley, J. L., and H. A. Panofsky, 1964: *The Structure of Atmospheric Turbulence.* Interscience, 239 pp.

Mahrt, L., 1991: Eddy asymmetry in the sheared heated boundary layer. *J. Atmos. Sci.,* **48,** 472–492.

——, and N. Gamage, 1987: Observations of turbulence in stratified flow. *J. Atmos. Sci.,* **44,** 1106–1121.

McFarlane, N. A., 1987: The effect of orographically excited gravity wave drag on the general circulation of the lower stratosphere and troposphere. *J. Atmos. Sci.,* **44,** 1775–1800.

Nappo, C. J., and G. Chimonas, 1991: Wave exchange between the ground surface and a boundary layer critical level. *J. Atmos. Sci.,*

Palmer, T. N., G. J. Shutts, and R. Swinbank, 1986: Alleviation of a systematic bias in general circulation and numerical weather prediction models through an orographic gravity wave drag parameterization. *Quart. J. Roy. Meteor. Soc.,* **112,** 1001–1039.

Peltier, W. R., and T. L. Clark, 1979: The evolution and stability of finite-amplitude mountain waves. Part II: Surface wave drag and severe downslope wind storms. *J. Atmos. Sci.,* **36,** 1498–1529.

Pierrehumbert, R. T., and B. Wyman, 1986: Upstream effects of mesoscale mountains. *J. Atmos. Sci.,* **42,** 977–1003.

Pitts, R. O., and T. J. Lyons, 1990: Air flow over a two-dimensional escarpment. II: Hydrostatic flow. *Quart. J. Roy. Meteor. Soc.,* **116,** 363–378.

Smith, R. B., 1977: The steepening of hydrostatic mountain waves. *J. Atmos. Sci.,* **34,** 1634–1654.

——, 1987: Aerial observation of the Yugoslavian bora. *J. Atmos. Sci.,* **44,** 269–297.

Smolarkiewicz, P. K., and R. Rotunno, 1989: Low Froude number flow past three-dimensional obstacles. Part I: Baroclinically generated lee vortices. *J. Atmos. Sci.,* **46,** 1154–1164.

Stern, W. F., and R. T. Pierrehumbert, 1988: The impact of an orographic gravity wave drag parameterization on extended range predictions with a GCM. *Eighth Conf. on Numerical Weather Prediction,* Amer. Meteor. Soc., 745–750.

Thorpe, S. A., 1973: Turbulence in stably stratified fluids: A review of laboratory experiments. *Bound.-Layer Meteor.,* **5,** 95–119.

Wyngaard, J., 1972: On surface layer turbulence. *Workshop on Micrometeorology,* Boston, D. A. Haugan, Ed., Amer. Meteor. Soc., 392 pp.